Electronic Supplementary Information

Experimental Section

Materials: Sodium gluconate ($C_6H_{11}NaO_7$, 99.0%), sodium carbonate (Na_2CO_3, 99.0%), hydrochloric acid (HCl, 99.0%), and ethanol (C_2H_6O, 99.0%), ammonium chloride (NH_4Cl), salicylic acid ($C_7H_6O_3$), sodium citrate dehydrate ($C_6H_5Na_3O_7 \cdot 2H_2O$), *p*-dimethylaminobenzaldehyde ($C_9H_{11}NO$), sodium nitroferricyanide dihydrate ($C_5FeN_6Na_2O \cdot 2H_2O$) and sodium hypochlorite solution (NaClO) were purchased from Aladdin Ltd. (Shanghai, China). Nafion (5 wt%) solution was purchased from Sigma-Aldrich Chemical Reagent Co., Ltd. Hydrochloric acid, nitric acid, sulfuric acid, hydrogen peroxide, hydrazine monohydrate ($N_2H_4 \cdot H_2O$) and ethyl alcohol (C_2H_5OH) were purchased from Beijing Chemical Corp. (China). chemical Ltd. in Chengdu. The ultrapure water used throughout all experiments was purified through a Millipore system. All reagents were analytical reagent grade without further purification.

Preparation of O-G: O-G was prepared as follows. In a typical synthesis, sodium gluconate (1.091 g) and Na_2CO_3 powder (10.599 g) were ground thoroughly in a 1:20 molar ratio using an agate mortar and pestle. The resulting mixture was placed in a corundum boat and transferred into a corundum tube mounted in a traditional horizontal tube furnace. After flushing with a flow of Ar for 30 min, the reactor was heated to 950 °C at a heating rate of 3 $°C \cdot min^{-1}$ and held at this temperature for 10 min. The system was then allowed to cool naturally to room temperature under a flow of Ar. To remove any remaining traces of the Na_2CO_3 salt, treatment with dilute hydrochloric acid was carried out. Finally, the pyrolysis products were washed with distilled water and absolute ethanol during vacuum filtration until the filtrate gave a neutral pH value, followed by drying at 80° C for 12 h. Another two control catalysts O-G-750 and O-G-1150 were also prepared under otherwide identical conditions, except by changing the annealing temperatures to

750 and 1150 °C.

Characterizations: XRD data were recorded using a LabX XRD-6100 X-ray diffractometer, with a Cu Kα radiation (40 kV, 30 mA) of wavelength 0.154 nm (SHIMADZU, Japan). TEM images were acquired on a HITACHI H-8100 electron microscopy (Hitachi, Tokyo, Japan) operated at 200 kV. XPS measurements were performed on an ESCALABMK II X-ray photoelectron spectrometer using Mg as the exciting source. FT-IR measurement was conducted by Thermo Fisher Nicolet iS10. EA data collected using a Elementar Vario EL cube. Raman spectra were obtained by a Renishaw inVia confocal Raman microprobe under 532 nm laser excitation. Absorbance spectra were acquired on SHIMADZU UV-1800 UV-Vis spectrophotometer. TPD data were collected using a TP-5076 multiple adsorption instrument. Briefly, 0.16 g of the catalyst was first pretreated with pure He at a flow rate of 30 $mL \cdot min^{-1}$ at 300 °C for 30 min, followed by cooling down to room temperature in the same atmosphere and then dosed with pure N_2. To remove residual N_2, the catalyst was purged with pure He at a flow rate of 30 $mL \cdot min^{-1}$ for 30 min. The N_2 TPD measurement was subsequently performed up to 600 °C at a heating rate of 10 $°C \cdot min^{-1}$ in pure He. A gas chromatograph (SHIMADZU, GC-2014C) equipped with MolSieve 5A column and Ar carrier gas was used for H_2 quantifications. ^1H NMR spectra were acquired on a 500 MHz Superconducting NMR spectrometer (Varian INOVA 500) and dimethyl sulphoxide was used as an internal to calibrate the chemical shifts in the spectra.

Electrochemical measurements: The reduction of N_2 gas (99.99%) was carried out in a two-compartment cell under ambient condition, which was separated by Nafion membrane. The membrane was protonated by first boiling in ultrapure water for 1 h and treating in H_2O_2 (5%) aqueous solution at 80 °C for another 1 h, respectively. And then, the membrane was treaded in 0.5 M H_2SO_4 for 3 h at 80 °C and finally in water for 6 h. The electrochemical experiments were carried out with an electrochemical workstation (CHI 660E). The potentials reported in this work were converted to reversible hydrogen electrode (RHE) scale via calibration with the following equation: E (RHE) = E (vs. Ag/AgCl) + 0.256 V and the presented current density was normalized to the geometric surface area. For electrochemical N_2 reduction, chrono-amperometry tests were conducted in N_2-saturated 0.1 M HCl solution (the HCl electrolyte was purged with N_2 for 30 min before the measurement).

Determination of NH_3: Concentration of produced NH_3 was spectrophotometrically determined by the indophenol blue method. 4 mL of sample was removed from the cathodic chamber, then added into 50 μL of oxidizing solution containing NaClO (ρ_{Cl} = 4~4.9) and NaOH (0.75 M), then added 500 μL coloring solution containing 0.4 M $C_6H_5Na_3O_7 \cdot 2H_2O$ and 0.32 M NaOH and 50 μL catalyst solution (0.1 g $Na_2[Fe(CN)_5NO] \cdot 2H_2O$ diluted to 10 ml with deionized water) in turn. Absorbance measurements were performed after one hour at λ = 660 nm. The concentration-absorbance curves were calibrated using standard NH_3 solution with a serious of concentrations. The fitting curve ($y = 0.3974x + 0.0735$, $R^2 = 0.999$) shows good linear relation of absorbance value with NH_3 concentration by three times independent calibrations.

Determination of N_2H_4: N_2H_4 presented in the electrolyte was estimated by the method of Watt and Chrisp. A mixed solution of 5.99 g $C_9H_{11}NO$, 30 mL HCl and 300 mL ethanol was used as a color reagent. Calibration curve was plotted as follow: firstly, preparing a series of standard solutions; secondly, adding 5 mL above prepared color reagent and stirring 20 min at room temperature; finally, the absorbance of the resulting solution was measured at 455 nm, and the yields of N_2H_4 were estimated from a standard curve using 5 mL residual electrolyte and 5 mL color reagent. Absolute calibration of this method was achieved using $N_2H_4 \cdot H_2O$ solutions of known concentration as standards, and the fitting curve shows good linear relation of absorbance with $N_2H_4 \cdot H_2O$ concentration ($y = 1.0002\, x + 0.0383$, $R^2 = 0.999$) by three times independent calibrations.

Determination of FE and V_{NH3}: FE for N_2 reduction was defined as the amount of electric charge used for synthesizing NH_3 divided the total charge passed through the electrodes during the electrolysis. The total amount of NH_3 produced was measured using colorimetric methods. Assuming three electrons were needed to produce one NH_3 molecule, the FE could be calculated as follows:

$FE = 3F \times c_{NH3} \times V / 17 \times Q$

V_{NH3} was calculated using the following equation:

$V_{NH3}= (c_{NH3} \times V) / (17 \times m)$

Where F is the Faraday constant, c_{NH3} is the measured NH_3 concentration, V is the volume of the HCl electrolyte for NH_3 collection, and t is the reduction time and $m_{cat.}$ is the catalyst mass.

Computational method: O-G models are built based on a 6×6 graphene sheet. All electron spin-polarized DFT methods implemented in the DMol3 module of Material Studio package have been employed for all present calculations.[1,2] The generalized gradient approximation Perdew-Burke-Ernzerhof (PBE) exchange-correlation functional is adopted.[3] The van der Waals interaction is described using the empirical correction scheme of Grimme.[4] To expand the electronic wavefunction, the double numerical plus polarization (DNP) basis set is used.[5] A 5 × 5 × 1 Monkhorst–Pack k-points are used in the DFT calculations. The vacuum layer about 20 Å is used between two neighboring slabs to avoid artificial interaction. Self-consistent field (SCF) calculations are performed with a total energy convergence criterion of 10^{-6} hartree. Since bulk water layer slightly stabilizes NRR intermediates,[6] we therefore adopted the conductor-like screening model (COSMO) to implicitly consider solvent effects.[7]

Six net coupled proton and electron transfer (CPET) steps are involved in the NRR ($N_2 + 6H^+ + 6e^- \rightarrow NH_3$). According to previous theoretical studies,[8] gaseous H_2 is employed as the proton source due to its convenience to simulate the anode reaction ($H_2 \leftrightarrow 2(H^+ + e^-)$). Each CPET step involves the transfer of a proton coupled with an electron from solution to an adsorbed species on the surface of electrocatalyst. The Gibbs free energy change (ΔG) of every elemental step is calculated by using the standard hydrogen electrode (SHE) model proposed by Nørskov et al.[9-11], which uses one-half of the chemical potential of hydrogen as the chemical potential of a coupled proton−electron pair. In detail, the free energy change is defined: $\Delta G = \Delta E + \Delta ZPE - T\Delta S + \Delta G_{pH} + \Delta G_{U}$, where ΔE is the reaction energy directly obtained from DFT calculations; ΔZPE is the change in zero-point energy; T is temperature (298.15 K); and ΔS is the change in entropy. $\Delta G_{U} = -neU$, where n is the number of electrons transferred and U is the electrode potential. ΔG_{pH} is the correction of the H^+ free energy by the concentration, which can be determined as $\Delta G_{pH} = 2.303 \times k_B T \times pH$ (or $0.059 \times pH$), where k_B is the Boltzmann constant and the value of pH was assumed to be zero. The zero-point energies and entropies of the NRR species are determined from the vibrational frequencies in which only the adsorbed species' vibrational modes are computed explicitly and the catalyst sheet was fixed. The entropies and vibrational frequencies of molecules in the gas phase are taken from the NIST database. [http://cccbdb.nist.gov/]

We also calculated adsorption energy of N_2/NNH on the catalyst sheet. The adsorption energy of X species $E_{ads}(X)$ is defined as the energy difference before and after the adsorption as

$$E_{ads}(X) = -\left[\, E(\text{total}) - E(\text{surface}) - E(X) \,\right]$$

where E(surface), E(X), and E(total) are the energies for the clean surface, X species in the gas phase, and X species adsorbed on the surface, respectively.

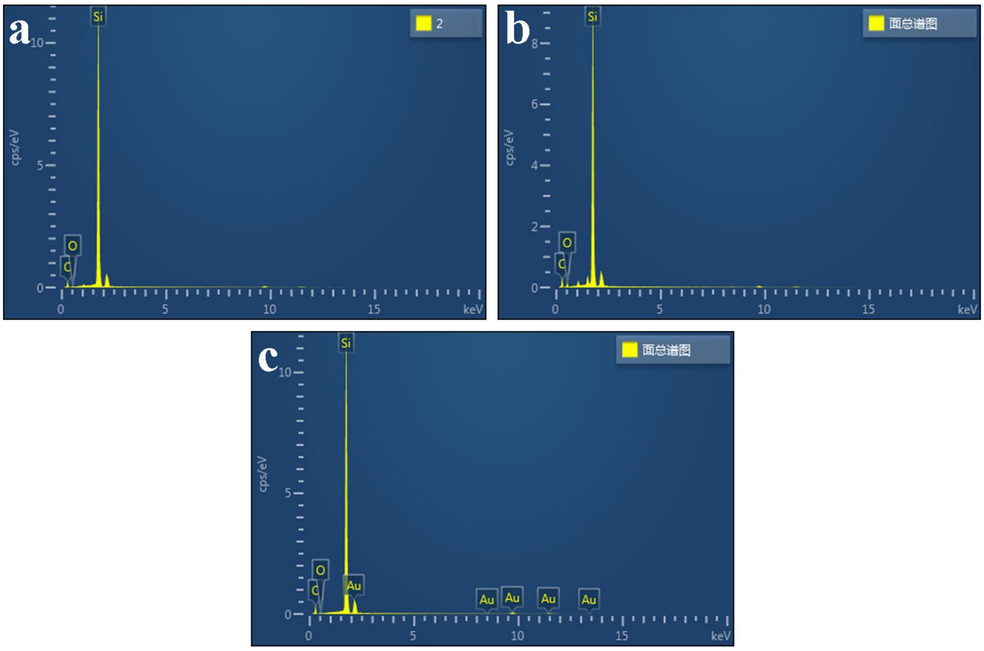

Fig. S1. EDX spectra of (a) O-G-750, (b) O-G, and (c) O-G-1150.

Table S1. Comparison of the total C content and the total O content for O-G, O-G-750, and O-G-1150.

catalysts	**C content (%)**	**O content (%)**
O-G	64.01	35.99
O-G-750	75.40	24.60
O-G-1150	89.33	10.67

Fig. S2. XPS survey spectra of O-G-750, O-G, and O-G-1150.

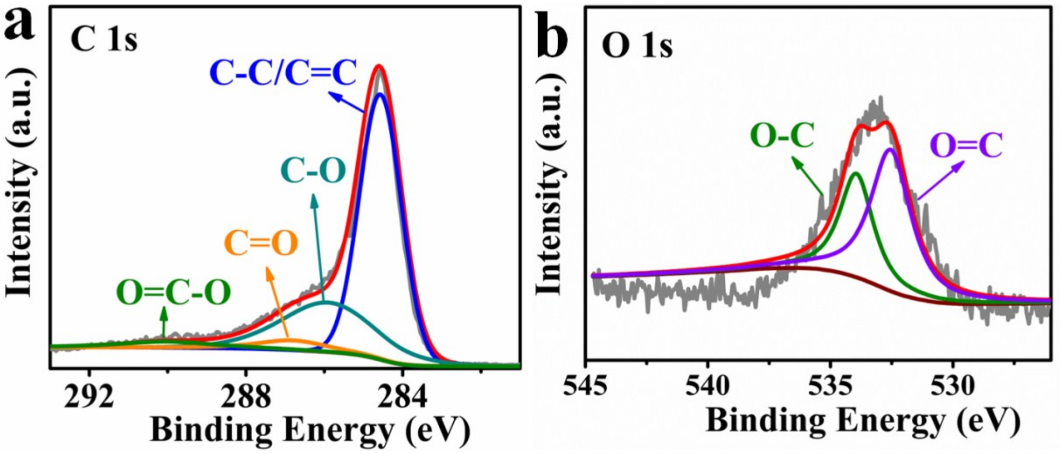

Fig. S3. XPS spectra of O-G-750 in the (a) C 1s and (b) O 1s regions.

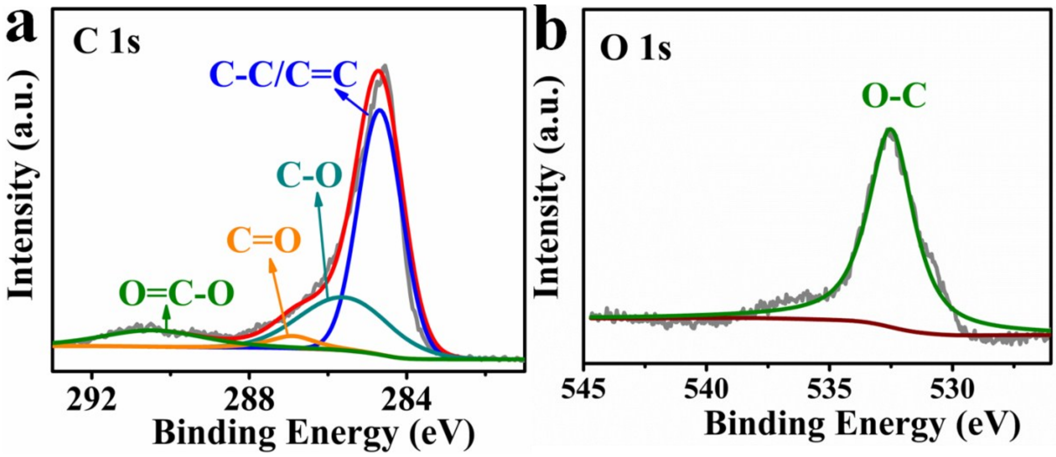

Fig. S4. XPS spectra of O-G-1150 in the (a) C 1s and (b) O 1s regions.

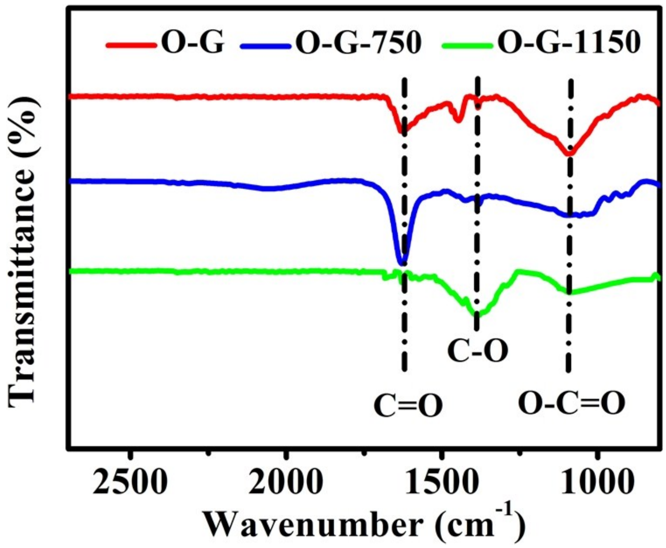

Fig. S5. FT-IR spectra of O-G, O-G-750, and O-G-1150.

Fig. S6. UV-Vis absorption spectra of indophenol assays with NH_4^+ ions after incubated for 2 h at room temperature and calibration curve used for estimation of NH_4^+.

Fig. S7. UV-Vis absorption spectra of various N_2H_4 concentrations after adding into chemical indicator by the method of Watt and calibration curve used for calculation of N_2H_4 concentrations.

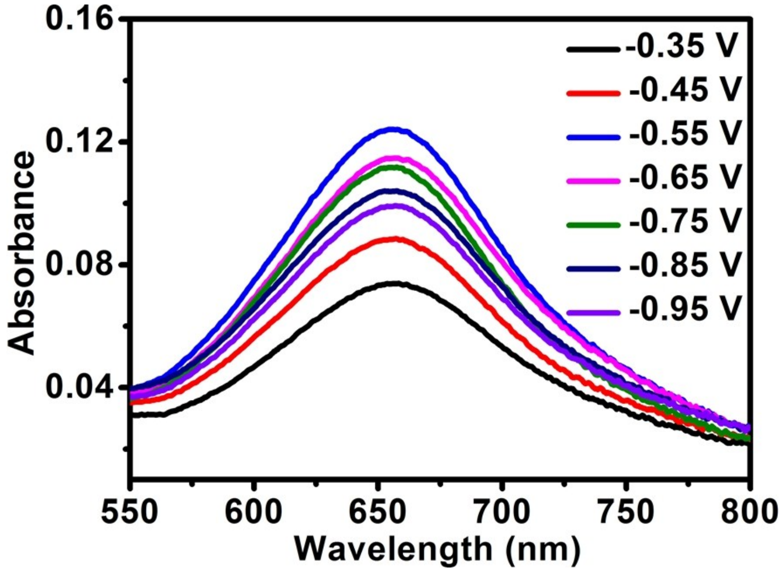

Fig. S8. The corresponding UV-Vis absorption spectra of the electrolytes stained with indophenol indicator at a series of potentials after electrolysis for 7200 s.

Fig. S9. UV-Vis absorption spectra of the electrolytes estimated by the method of Watt and Chrisp before and after 2-h electrolysis in N_2 atmosphere at each given potential at ambient conditions using O-G/CP as the working electrode.

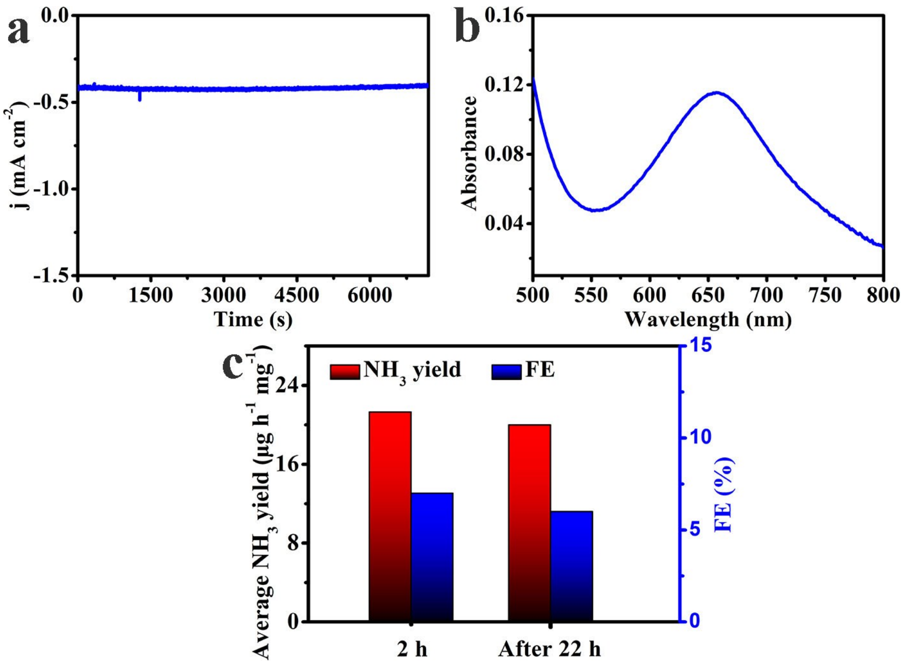

Fig. S10. (a) Time-dependent current density curves over O-G/CP at –0.55 V for 7200 s in 0.1 M HCl after 22 h stability test. (b) The corresponding UV-Vis absorption spectra of the electrolytes stained with indophenol indicator at –0.55 V after electrolysis for 7200 s. (c) NH_3 yields and FEs after charging at –0.55 V for 2 and after 22 h.

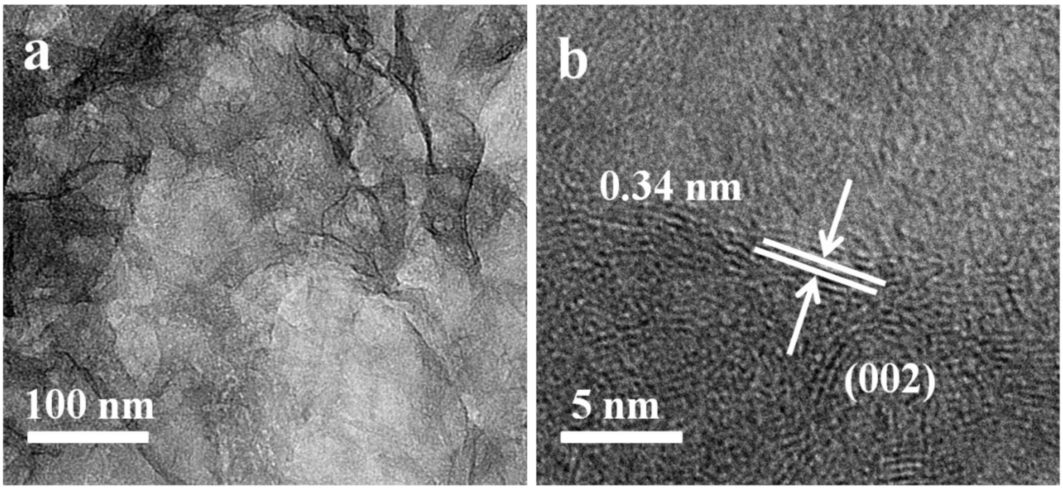

Fig. S11. (a) TEM and (b) HRTEM images for O-G after stability test.

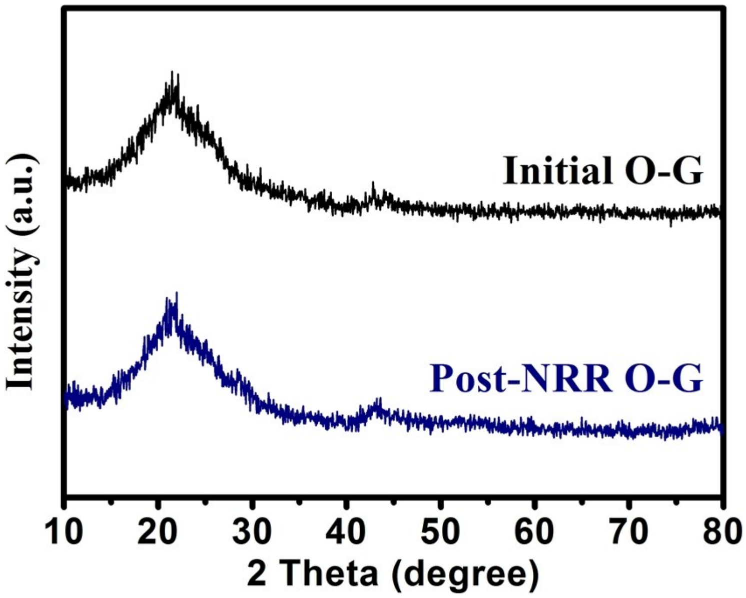

Fig. S12. XRD patterns for initial O-G and post-NRR O-G.

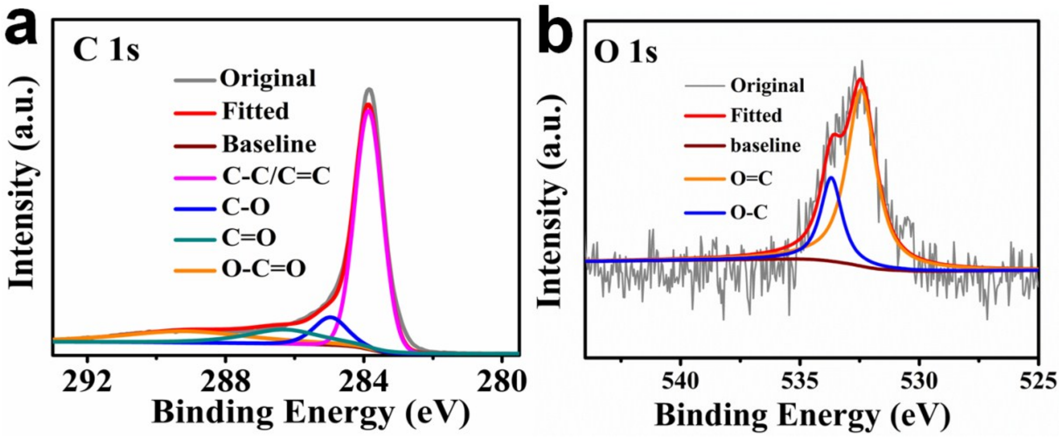

Fig. S13. XPS spectra of O-G in the (a) C 1s and (b) O 1s regions after stability test.

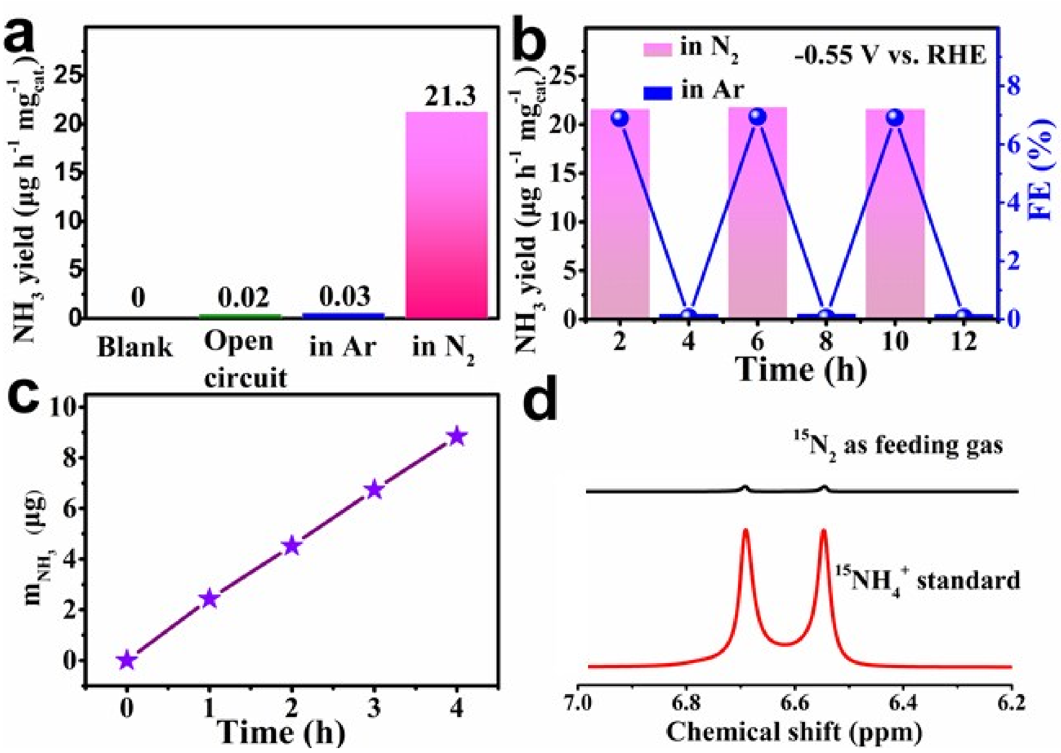

Fig. S14. (a) NH_3 yields of before (blank) and after 2 h electrolysis under different conditions: open circuit in N_2, –0.55 V in Ar, and –0.55 V in N_2. (b) NH_3 yields (left y-axis) and FEs (right y-axis) of O-G at –0.55 V with alternating 2-h cycles between N_2-saturated and Ar-saturated electrolytes, for a total of 12 h. (c) Amount of NH_3 vs. reaction time at –0.55 V over O-G/CP. (d) ^{1}H NMR spectrum for the post-electrolysis 0.1 M HCl electrolytes with $^{15}N_2$ as the feeding gas. Also shown is the spectrum for $^{15}NH_4^+$ standard sample.

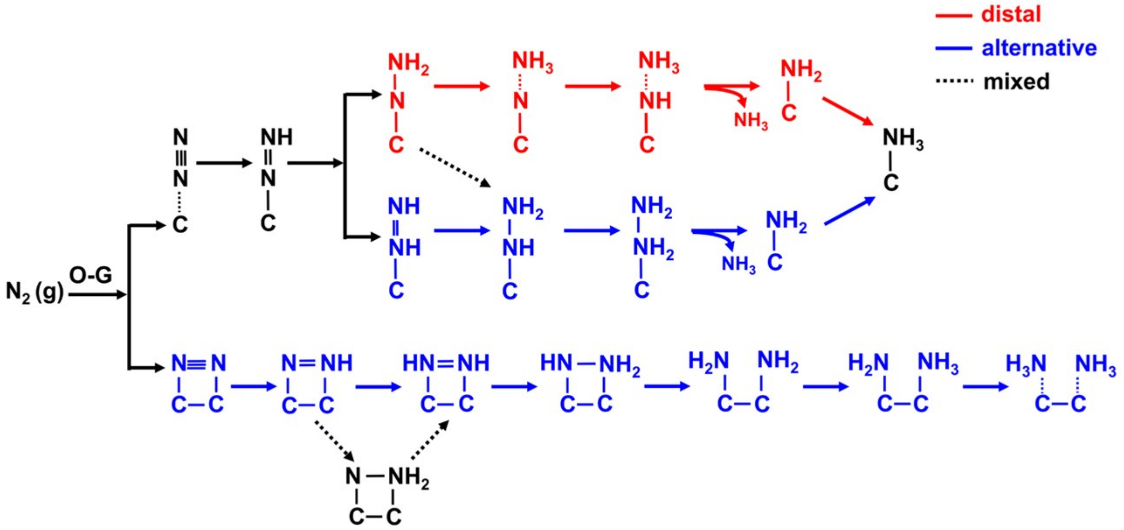

Scheme S1. Scheme for the alternative, distal, and mixed associative mechanisms for the N_2 electroreduction to NH_3 catalyzed by O-G.

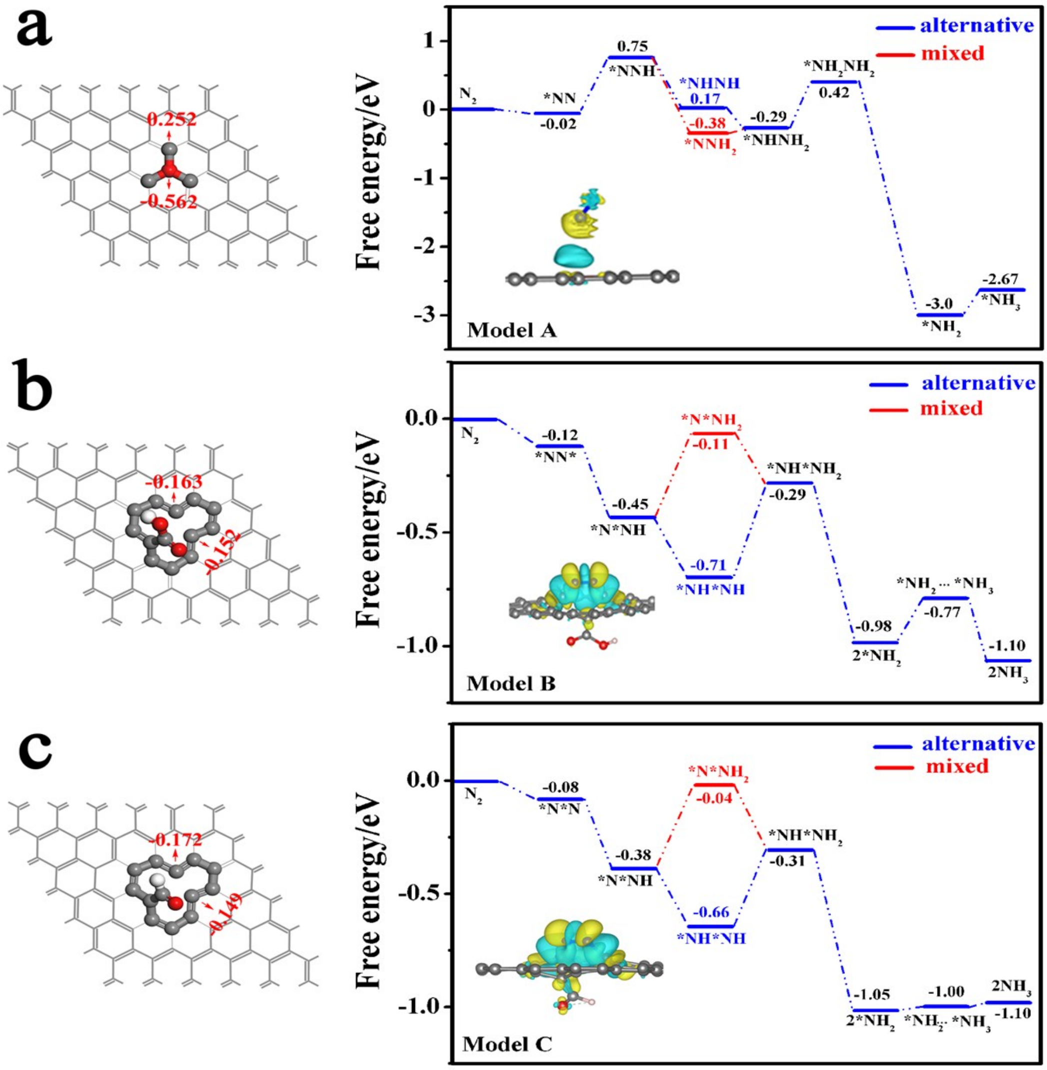

Fig. S15. Slab models used in this work and related NRR mechanisms (a, model A; b, model B; c, model C). Also shown are charge differences upon N_2 adsorption.

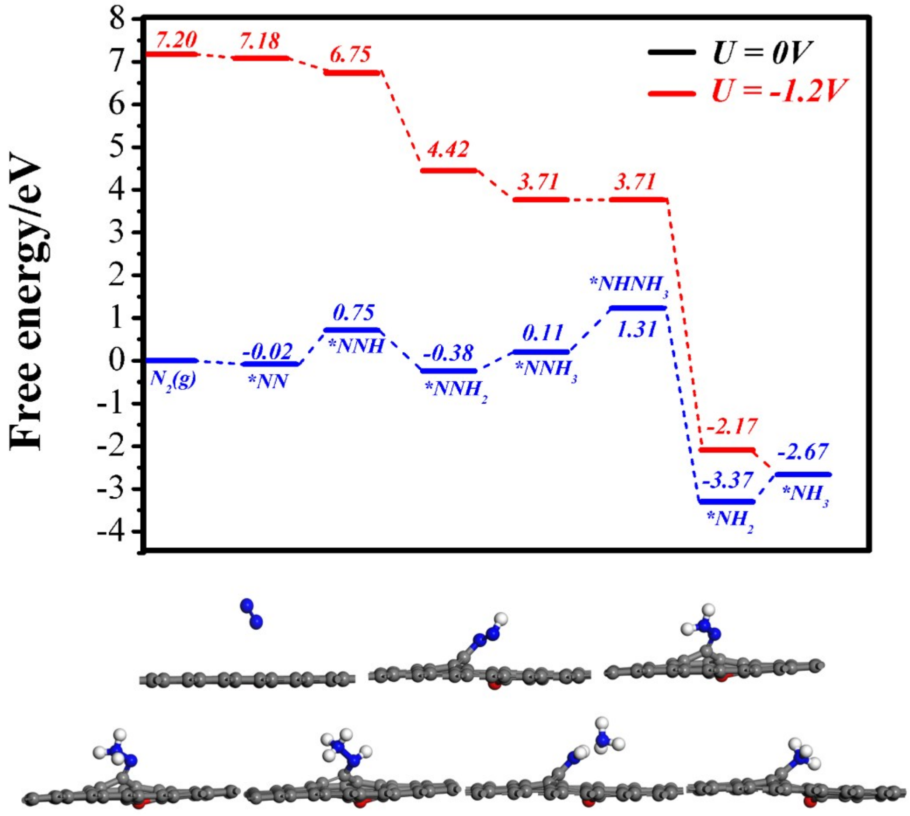

Fig. S16. DFT calculated NRR mechanisms (in eV) and optimized geometric structures of the NRR intermediates of Model A (distal pathway). Color code: carbon in gray, oxygen in red, hydrogen in white.

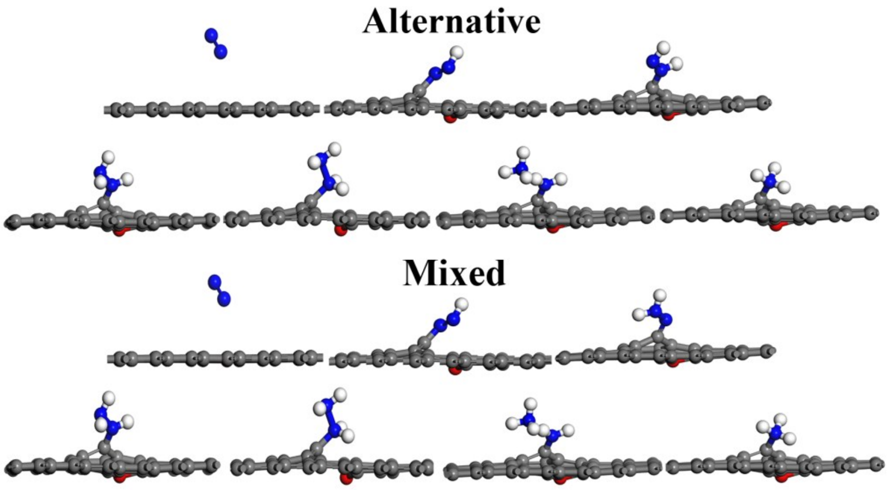

Fig. S17. DFT optimized geometric structures of the NRR intermediates of Model A (alternative and mixed pathway). Color code: carbon in gray, oxygen in red, hydrogen in white.

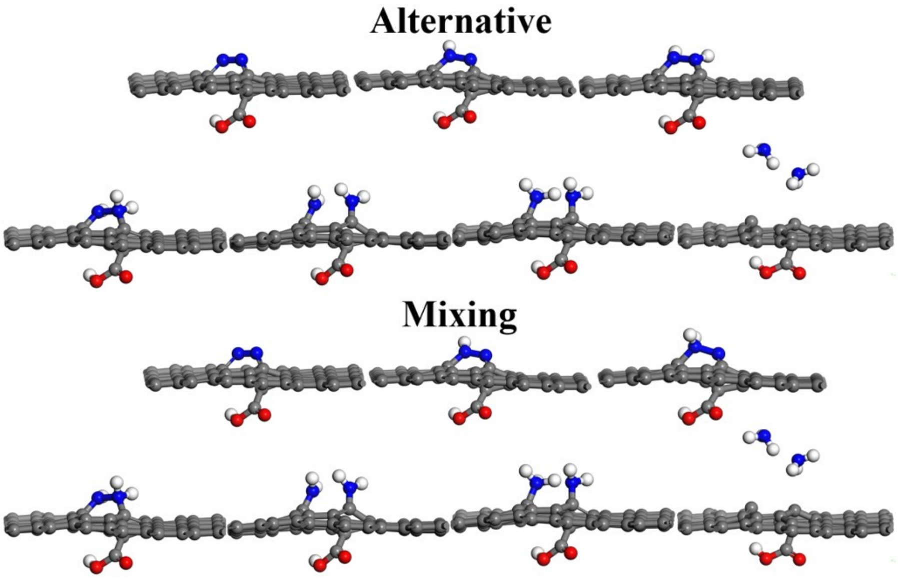

Fig. S18. DFT optimized geometric structures of the NRR intermediates of Model B (alternative and mixed pathway). Color code: carbon in gray, oxygen in red, hydrogen in white.

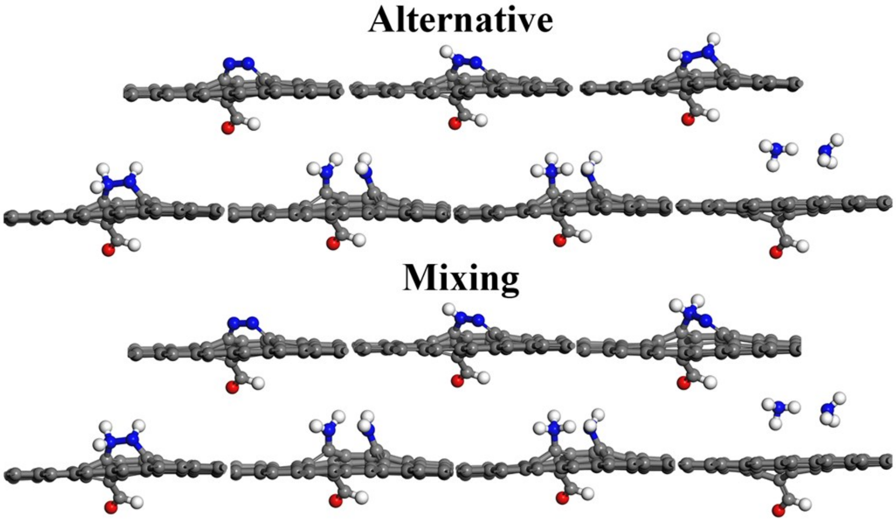

Fig. S19. DFT optimized geometric structures of the NRR intermediates of Model C (alternative and mixed pathway). Color code: carbon in gray, oxygen in red, hydrogen in white.

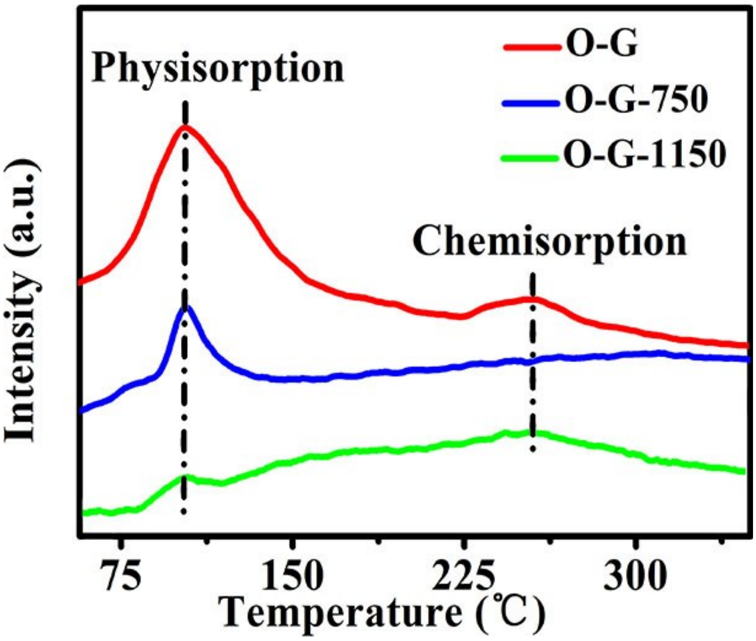

Fig. S20. N_2 TPD curves of O-G, O-G-750, and O-G-1150.

Table S2. Comparison of electrocatalytic NRR performance for O-G with other electrocatalysts under ambient conditions.

Catalyst	**Electrolyte**	**NH_3 yield**	**FE (%)**	**Ref.**
O-G/CP	0.1 M HCl	21.3 μg h^{-1} $mg^{-1}_{cat.}$	12.6	This work
TA-reduced Au/TiO_2	0.1 M HCl	21.4 μg h^{-1} $mg^{-1}_{cat.}$	8.11	12
α-Au/CeO_x-RGO	0.1 M HCl	8.31 μg h^{-1} $mg^{-1}_{cat.}$	10.1	13
Au nanorods	0.1 M KOH	6.04 μg h^{-1} $mg^{-1}_{cat.}$	4	14
AuHNCs	0.5 M $LiClO_4$	3.90 μg h^{-1} cm^{-2}	30.2	15
Ru/C	2 M KOH	0.21 μg h^{-1} cm^{-2}	0.28	16
$Bi_4V_2O_{11}$/CeO_2	0.1 M HCl	23.21 μg h^{-1} $mg^{-1}_{cat.}$	10.16	17
MoS_2	0.1 M Na_2SO_4	0.02 μg h^{-1} cm^{-2}	1.17	18
Mo nanofilm	0.01 M H_2SO_4	1.89 μg h^{-1} cm^{-2}	0.72	19
PEBCD/C	0.5 M Li_2SO_4	1.58 μg h^{-1} cm^{-2}	2.85	20
Fe_2O_3-CNT	$KHCO_3$	0.22 μg h^{-1} cm^{-2}	0.15	21
N-doped nanocarbon	0.05 M H_2SO_4	27.20 μg h^{-1} $mg^{-1}_{cat.}$	1.42	22
ZIF-derived carbon	0.1 M KOH	57.8 μg h^{-1} cm^{-2}	10.20	23
N-doped carbon	0.1 M HCl	15.7 μg h^{-1} $mg^{-1}_{cat.}$	1.45	24
polymeric carbon nitride	0.1 M HCl	8.09 μg h^{-1} $mg^{-1}_{cat.}$	11.59	25
boron-doped graphene	0.05 M H_2SO_4	9.8 μg h^{-1} cm^{-2}	10.8	26
MoO_3	0.1 M HCl	29.43 μg h^{-1} $mg^{-1}_{cat.}$	1.9	27
Mo_2N nanorod	0.1 M HCl	78.4 μg h^{-1} $mg^{-1}_{cat.}$	4.5	28
MoN	0.1 M HCl	3.01×10^{-10} mol s^{-1} cm^{-2}	1.15	29
VN	0.1 M HCl	8.40×10^{-11} mol s^{-1} cm^{-2}	2.25	30
Nb_2O_5 nanofiber	0.1 M HCl	43.6 μg h^{-1} $mg^{-1}_{cat.}$	9.26	31

hollow Cr_2O_3 microspheres	0.1 M Na_2SO_4	25.3 μg h^{-1} $mg^{-1}_{cat.}$	6.78	32
TiO_2-rGO	0.1 M Na_2SO_4	15.13 μg h^{-1} $mg^{-1}_{cat.}$	3.3	33
Fe_2O_3 nanorods	0.1 M Na_2SO_4	15.9 μg h^{-1} $mg^{-1}_{cat.}$	0.94	34
defect-rich MoS_2 nanoflower	0.1 M Na_2SO_4	29.28 μg h^{-1} $mg^{-1}_{cat.}$	8.34	35
B_4C	0.1 M HCl	26.57 μg h^{-1} $mg^{-1}_{cat.}$	15.95	36
oxygen-doped carbon nanosheet	0.1 M HCl	20.15 μg h^{-1} $mg^{-1}_{cat.}$	4.97	37
oxygen-doped hollow carbon microtubes	0.1 M HCl	25.12 μg h^{-1} $mg^{-1}_{cat.}$	9.1	38

Table S3. Comparison of the content of carbon element for the electrolyte both before and after NRR test by Element Analysis.

	C (%)
Initial	0.07
Post-NRR	0.04

Table S4. Comparison of NH_3 yield and FE for O-G, O-G-750, and O-G-1150 under ambient conditions.

catalysts	**NH_3 yield**	**FE (%)**
O-G	21.3 $\mu g\ h^{-1}\ mg^{-1}{}_{cat.}$	12.6
O-G-750	7.5 $\mu g\ h^{-1}\ mg^{-1}{}_{cat.}$	4.5
O-G-1150	11.8 $\mu g\ h^{-1}\ mg^{-1}{}_{cat.}$	6.4

References

1 B. Delley, *J. Chem. Phys.*, 1990, **92**, 508–517.

2 B. Delley, *J. Chem. Phys.*, 2000, **113**, 7756–7764.

3 J. P. Perdew, K. Burke and M. Ernzerhof, *Phys. Rev. Lett.*, 1996, **77**, 3865.

4 S. Grimme, *J. Comput. Chem.*, 2006, **27**, 1787–1799.

5 P. Liu, J. A. Rodriguez, *J. Am. Chem. Soc.*, 2005, **127**, 14871–14878.

6 E. Skúlason, T. Bligaard, S. Gudmundsdóttir, F. Studt, J. Rossmeisl, F. A. Pedersen, T. Vegge, H. Jónsson and J. K. Nørskov, *Phys. Chem. Chem. Phys.*, 2012, **14**, 1235–1245.

7 A. Klamt, G. Schüürmann, *J. Chem. Soc., Perkin Trans. 2,* 1993, **0**, 799–805.

8 K. C. MacLeod, S. F. McWilliams, B. Q. Mercado and P. L. Holland, *Chem. Sci.*, 2016, **7**, 5736–5746.

9 J. K. Nørskov, J. Rossmeisl, A. Logadottir and L. Lindqvist, *J. Phys. Chem. B*, 2004, **108**, 17886–17892.

10 J. Rossmeisl, A. Logadottir and J. K. Nørskov, *Chem. Phys.*, 2005, **319**, 178–184.

11 A. A. Peterson, F. Abild-Pedersen, F. Studt, J. Rossmeisl and J. K.Nørskov, *Energy Environ. Sci.*, 2010, **3**, 1311–1315.

12 M. Shi, D. Bao, B. Wulan, Y. Li, Y. Zhang, J. Yan and Q. Jiang, *Adv. Mater.*, 2017, **29**, 1606550.

13 S. Li, D. Bao, M. Shi, B. Wulan, J. Yan and Q. Jiang, *Adv. Mater.*, 2017, **29**, 1700001.

14 D. Bao, Q. Zhang, F. Meng, H. Zhong, M. Shi, Y. Zhang, J. Yan, Q. Jiang and X. Zhang, *Adv. Mater.*, 2017, **29**, 1604799.

15 M. Nazemi, S. R. Panikkanval and M. A. El-Sayed, *Nano Energy,* 2018, **49**, 316–323.

16 V. Kordali, G. Kyriacou and C. Lambrou, *Chem. Commun.*, 2000, **17**, 1673–1674.

17 C. Lv, C. Yan, G. Chen, Y. Ding, J. Sun and Y. Zhou, G. Yu, *Angew. Chem.*, *Int. Ed.*, 2018, **130**, 6181–6184.

18 L. Zhang, X. Ji, X. Ren, Y. Ma, X. Shi, Z. Tian, A. M. Asiri, L. Chen, B. Tang and X. Sun, *Adv. Mater.*, 2018, **30**, 1800191.

19 D. Yang, T. Chen and Z. Wang, *J. Mater. Chem. A*, 2017, **5**, 18967–18971.

20 G.-F. Chen, X. Cao, S. Wu, X. Zeng, L. Ding, M. Zhu and H. Wang, *J. Am. Chem. Soc.*, 2017, **139**, 9771–9774.

21 S. Chen, S. Perathoner, C. Ampelli, C. Mebrahtu, D. Su and G. Centi, *Angew. Chem.*,

Int. Ed., 2017, **56**, 2699–2703.

22 Y. Liu, Y. Su, X. Quan, X. Fan, S. Chen, H. Yu, H. Zhao, Y. Zhang and J. Zhao, *ACS Catal.*, 2018, **8**, 1186–1191.

23 S. Mukherjee, D. A. Cullen, S. Karakalos, K. Liu, H. Zhang, S. Zhao, H. Xu, K. L. More, G. Wang and G. Wu, *Nano Energy*, 2018, **48**, 217–226.

24 X. Yang, K. Li, D. Cheng, W. Pang, J. Lv, X. Chen, H. Zang, X. Wu, H. Tan, Y. Wang and Y. Li, *J. Mater. Chem. A*, 2018, **6**, 7762–7769.

25 C. Lv, Y. Qian, C. Yan, Y. Ding, Y. Liu, G. Chen and G. Yu, *Angew. Chem., Int. Ed.*, 2018, **57**, 10246–10250.

26 X. Yu, P. Han, Z. Wei, L. Huang, Z. Gu, S. Peng, J. Ma and G. Zheng, *Joule*, 2018, **2**, 1610–1622.

27 J. Han, X. Ji, X. Ren, G. Cui, L. Li, F. Xie, H. Wang, B. Li and X. Sun, *J. Mater. Chem. A*, 2018, **6**, 12974–12977.

28 X. Ren, G. Cui, L. Chen, F. Xie, Q. Wei, Z. Tian and X. Sun, *Chem. Commun.*, 2018, **54**, 8474–8477.

29 L. Zhang, X. Ji, X. Ren, Y. Luo, X. Shi, A. M. Asiri, B. Zheng and X. Sun, *ACS Sustainable Chem. Eng.*, 2018, **6**, 9550–9554.

30 R. Zhang, Y. Zhang, X. Ren, G. Cui, A. M. Asiri, B. Zheng and X. Sun, *ACS Sustainable Chem. Eng.*, 2018, **6**, 9545–9549.

31 J. Han, Z. Liu, Y. Ma, G. Cui, F. Xie, F. Wang, Y. Wu, S. Gao, Y. Xu and X. Sun, *Nano Energy*, 2018, **52**, 264–270.

32 Y. Zhang, W. Qiu, Y. Ma, Y. Luo, Z, Tian, G. Cui, F. Xie, L. Chen, T. Li and X. Sun, *ACS Catal.*, 2018, **8**, 8540–8544.

33 X. Zhang, Q. Liu, X. Shi, A. M. Asiri, Y. Luo, X. Sun and T. Li, *J. Mater. Chem. A*, 2018, **6**, 17303–17306.

34 X. Xiang, Z. Wang, X. Shi, M. Fan and X. Sun, *ChemCatChem*, 2018, **10**, 4530–4535.

35 X. Li, T. Li, Y. Ma, Q. Wei, W. Qiu, H. Guo, X. Shi, P. Zhang, A. M. Asiri, L. Chen, B. Tang and X. Sun, *Adv. Energy Mater.*, 2018, **8**, 1801357.

36 W. Qiu, X. Xie, J. Qiu, W. Fang, R. Liang, X. Ren, X. Ji, G. Cui, A. M. Asiri, G. Cui, B. Tang and X. Sun, *Nat. Commun.*, 2018, **9**, 3485.

37 H. Huang, L. Xia, R. Cao, Z. Niu, H. Chen, Q. Liu, T. Li, X. Shi, A. M. Asiri and X. Sun, *Chem. Eur. J.*, 2018, **25**, 1914–1917.

38 T. Wu, P. Li, H. Wang, R. Zhao, Q. Zhou, W. Kong, M. Liu, Y. Zhang, X. Sun and F.

Gong, *Chem. Commun.*, 2019, **55**, 2684–2687.